Wind and Structures, *Vol. 24, No. 4 (2017) 333-350*
DOI: https://doi.org/10.12989/was.2017.24.4.333

Monitoring system for the wind-induced dynamic motion of 1/100-scale spar-type floating offshore wind turbine

C.M. Kim[1], J.R. Cho[*2], S.R. Kim[1] and Y.S. Lee[2]

[1]*Korea Institute of Industrial Engineering, Gangseo-Gu, Busan 618-230, Korea*
[2]*Naval Architecture and Ocean Engineering, Hongik University, Sejong 339-701, Korea*

(Received February 8, 2016, Revised October 7, 2016, Accepted October 11, 2016)

Abstract. Differing from the fixed-type, the dynamic motion of floating-type offshore wind turbines is very sensitive to wind and wave excitations. Thus, the sensing and monitoring of its motion is important to evaluate the dynamic responses to the external excitation. In this context, a monitoring system for sensing and processing the wind-induced dynamic motion of spar-type floating offshore wind turbine is developed in this study. It is developed by integrating a 1/00 scale model of 2.5MW spar-type floating offshore wind turbine, water basin equipped with the wind generator, sensing and data acquisition systems, real-time CompactRIO controller and monitoring program. The scale model with the upper rotatable blades is installed within the basin by means of three mooring lines, and its translational and rotational motions are detected by 3-axis inclinometer and accelerometers and gyroscope. The detected motion signals are processed using a real-time controller CompactRIO to calculate the acceleration and tilting angle of nacelle and the attitude of floating platform. The developed monitoring system is demonstrated and validated by measuring and evaluating the time histories and trajectories of nacelle and platform motions for three different wind velocities and for eight different fairlead positions.

Keywords: wind turbine; spar-type floating offshore; monitoring system; 1/100 scale model; wind-induced motion and trajectory; wind velocity; fairlead position

1. Introduction

The reliance upon renewable energies is continuously increasing all over the world as fossil energies are getting exhausted, and particularly wind energy is considering as a leading renewable energy source in aspects of its massive scale and high efficiency. To extract the renewable energy from the wind, wind turbines were initially installed on land and showed the rapid increase in both the total installation number and the maximum wind power capacity. However, owing to the lack of allowable installation sites on land, their growth was limited and the attention is naturally turning to the offshore sites, a less restrictive installation place. In offshore wind turbines, the fixed-type that is supported by jacket or monopile is relatively favorable in aspects of the easy installation and dynamic stability, but the environmental infringement and the limitation of large-scale still remain troublesome problem because those are limited to the costal sites. Thus, the floating-type offshore wind turbines that can be

*Corresponding author, Professor, E-mail: jrcho@hongik.ac.kr

http://www.techno-press.com/journals/was&subpage=7 ISSN: 1226-6116 (Print), 1598-6225 (Online)

installed at deep sea are recently highlighted for increasing the penetration rate of wind energy (Musial and Butterfield 2004, Breston and Noe 2009, Karimirad 2014).

However, differing from the fixed-type, the floating-type offshore wind turbines are sensitive to wind and wave loads in aspects of the station keeping and the vertical position stability because those are supported by the floating substructure. And, the dynamic behavior of floating offshore wind turbines is determined how well the station keeping and the vertical position are secured (Ton 1998, Faltinsen 1990). Even thought there is a little difference depending on the type of floating substructure, the dynamic stability is maintained by a combination of buoyancy force, the tension of mooring lines or tension legs, the metacentric height and additional control devices (Koo *et al*. 2004, Cowell and Basu 2009). In case of spar-type floating offshore wind turbine, it has been reported (Lee 2008, Jeon *et al*. 2013) that the fairlead location and the total length and pre-tension of mooring lines are also additional important factors for securing the dynamic stability. In this context, the evaluation of dynamic responses of floating offshore wind turbine to wind and wave loads is prerequisite for the design of dynamically stable floating offshore wind turbine. To investigate the parametric dynamics responses to the above-mentioned key parameters, the numerical approaches have been widely adopted (Jonkman and Buhl 2007, Lee 2005, Waris and Ishihara 2012, Karimirad and Moan 2012) because those are not restricted by the geometric scale of wind turbine. However, a common critical issue in the numerical approach is the reliability assurance of numerical results owing to the limitation and uncertainty in the modeling and simulation, and therefore its verification using experiment should be made (Jonkman 2009).

A common feature of the experiments is the use of the scale model because of the limitation of full-scale field test. Not only the construction of full-scale model and experiment apparatus is impractical in aspects of technology and cost, but the test site and the test conditions are extremely restrictive. Even for the scale model experiment, the elaborative considerations should be made for generating the wave/wind loads and setting up the sensor/data acquisition system as well as for scaling down the wind turbine. Nielsen *et al*. (2006) carried out the scale model experiments for the Hywind concept for floating offshore wind turbines to compare the simulation results for a variety of environmental and control conditions. Frye *et al*. (2011) designed a 1/100 scale model of spar floating wind turbine and tested the dynamic response using a water tank, and Martin (2011) developed a 1/50 scale model of NREL 5MW floating offshore wind turbine and tested the major performances using a wave basin equipped with wind generator and compared with the analytical results. Utsunomiya *et al*. (2013) performed the at-sea experiment using a 1/10-scale model of hybrid spar floating offshore wind turbine, in order to compare the spar motion, mooring tension and structural strain between the numerical simulation and experiment. Choi *et al.* (2015) carried out the wave-tank experiment using a simplified 1/75 spar floating platform and compared the RAOs of platform motion and mooring tension with the coupled FSI simulation.

The scale-model experiment technology has been settled down to some extent thanks to the worldwide extensive research efforts, however it still remains further advancement in several aspects, for example, the measuring of wind-induced dynamic response and its monitoring using the scale model. As an extension of our previous numerical and experimental studies on the dynamic responses of spar-type floating platform (Jeon *et al*. 2013, Choi *et al*. 2015), this study intends to develop a monitoring system for the wind-induced dynamic motion of spar-type floating offshore wind turbine. A 1/100 scale model of 2.5MW spar-type floating offshore wind turbine including the upper rotatable blades and a water basin equipped with the wind generator are designed. And, the motion monitoring system is developed by integrating the motion sensors, data acquisition/processing systems and real-time CompactRIO controller. The acceleration and tilting angle of nacelle and the attitude of floating platform are detected by the motion sensors, and the detected motion signals are processed using a real-time CompactRIO controller. Using the developed system, the time histories and trajectories of nacelle and platform motions are measured, monitored and evaluated with respect to the wind velocity and the fairlead position.

2. Spar-type floating offshore wind turbine

Fig. 1(a) shows a typical spar-type floating offshore wind turbine which is composed of rotor blades, nacelle, tower and floating platform. The wind turbine is moored by three catenary mooring cables which are anchored at seabed and connected to the fairlead of floating platform. The key parameters and the six rigid body motions of floating platform are represented. Where, z_{FL}, z_{CB} and z_{CG} indicate the vertical positions of fairlead, center of buoyancy and center of gravity, respectively. The dynamic stability of floating offshore wind turbine is meant by the station keeping at sea, the stability of vertical posture, and it is quantitatively evaluated in terms of six rigid body motions. The station keeping is mostly secured by the tension of three mooring cables, while the vertical posture is controlled by the vertical stiffness of floating platform that is influenced by several factors such as the metacentric height, the fairlead position, the bottom control weight and passive/active control device. The dynamic stability of floating platform may not only influence the structural safety of whole wind turbine, but it may also degrade the wind power efficiency because of the misalignment of rotor blades to the wind direction. Thus, the securing of dynamic stability becomes the first and most important subject in the design of spar-type floating offshore wind turbine.

The dynamic behavior of wind turbine is greatly influenced by wind load, which becomes more serious when wind turbine is not fixed on ground but floating at sea. Differing from the fixed-type in which the wind-induced dynamic forces and moments are firmly supported by wind tower, the station keeping and the vertical posture of floating-type could be maintained by the elaborate control of the flexible mooring lines and the associated parameters and devices. Thus, the

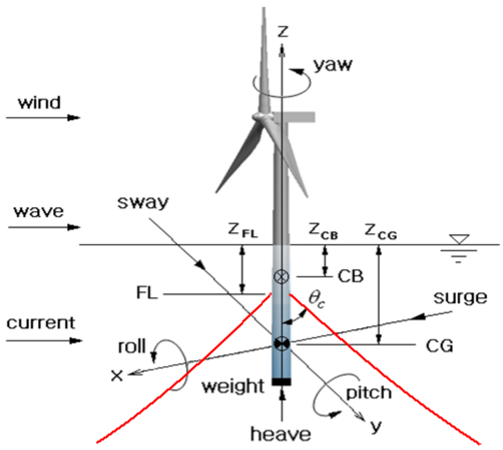

(a)

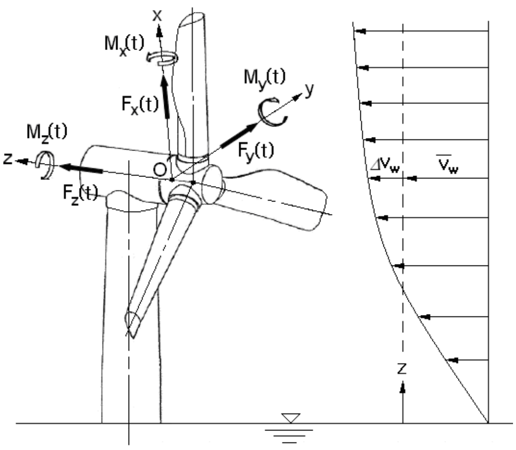

(b)

Fig. 1 Spar-type floating offshore wind turbine: (a) 6-DOF rigid body motions (CB: center of buoyancy, CG: center of gravity, FL: fairlead), (b) wind-induced dynamic forces and moments translational and rotational motions of floating wind turbine can be significantly influenced by wind load. The situation becomes more crucial when the wind load is unstable and its profile is abnormal (Torrance 1972). In most cases, the wind profile is not uniform in both the vertical and lateral directions, and furthermore the wind direction is inclined to the rotor axis. Owing to this characteristic of wind profile, the wind-induced dynamic forces and moments acting on the wind turbine are usually decomposed into six components, as represented in Fig. 1(b). Where, $M_x(t)$ denotes the dynamic driving toque that is delivered to the gear transmission system by the rotation of rotor blades, and $M_x(t)$ and $M_y(t)$ are mostly produced by the difference in the wind pressure distributions on three rotor blades owing to the non-uniform wind profile in the lateral direction. Meanwhile, $F_z(t)$ is due to the total axial dynamic pressure of wind, and $F_x(t)$ and $F_y(t)$ are due to the wind flow components which are inclined to the rotor axis.

Meanwhile, the dynamic motion of floating platform is interacted with the wave flow and the cable dynamics. By denoting $\{\boldsymbol{U},\theta\}$ be its rigid body translation and rotation at the center of mass, the dynamic motion of the floating platform is governed by the conservation of linear and angular momentums

$$m\{\ddot{\boldsymbol{U}}\}+[\boldsymbol{c}]\{\dot{\boldsymbol{U}}\}+[\boldsymbol{k}]\{\boldsymbol{U}\}=\{\boldsymbol{F}\} \tag{1}$$

$$\left[\boldsymbol{I}^{\theta}\right]\ddot{\boldsymbol{\theta}}+\left[\boldsymbol{c}^{\theta}\right]\dot{\boldsymbol{\theta}}+\left[\boldsymbol{k}^{\theta}\right]\boldsymbol{\theta}=\boldsymbol{M} \tag{2}$$

with the notation convention $[\boldsymbol{A}]=diag(A_x,A_y,A_z)$ for four matrices $[\boldsymbol{c}],[\boldsymbol{k}],\left[\boldsymbol{c}^{\theta}\right]$ and $\left[\boldsymbol{k}^{\theta}\right]$. Here, m,c_i,k_i,c_i^{θ} and k_i^{θ} denote the total mass and the damping and stiffness coefficients for the translational and rotational degrees of freedom, respectively. And, $\left[\boldsymbol{I}^{\theta}\right]$ indicates the matrix of mass moments of inertia with respect to the center of mass, and ***F*** and ***M*** are the pressure-induced external force and moment vectors.

Meanwhile, mooring cables of length L are a slender flexible structure subject to hydrodynamic pressure, self-weight, inertia and drag forces. Referring to Fig. 2(b), the nonlinear differential equations of motion (Goodman and Breslin 1976, Aamo and Fossen 2000) for the

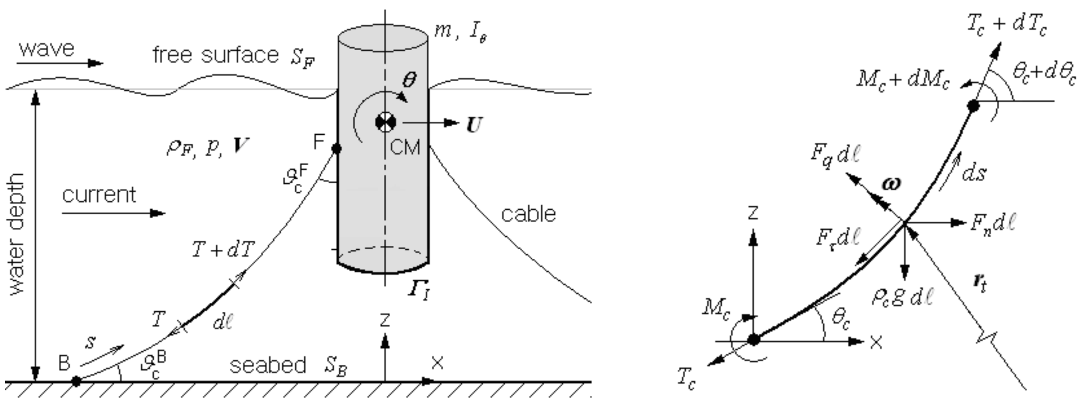

(a) (b)

Fig. 2 (a) A moored rigid spar floating platform, (b) forces acting on the cable element $d\ell$

differential cable element with the length $d\ell$ are governed by the equilibrium equations in translation and rotation

$$(m_c + m_a)\frac{\partial \dot{\boldsymbol{u}}_c}{\partial t} = \frac{\partial \boldsymbol{T}_c}{\partial s} + (1+\gamma)\boldsymbol{F_c} \tag{3}$$

$$\frac{\partial \boldsymbol{M_c}}{\partial s} = -\boldsymbol{r_t} \times (1+\gamma)\boldsymbol{T_c} \tag{4}$$

In which, m_c indicates the mass per unit arc length, m_a the added mass of water, $\dot{\boldsymbol{u}}_{\boldsymbol{c}}$ the velocity vector, s the arc length of unstressed cable, and γ the engineering strain. In addition, $\boldsymbol{r_t}$ is the vector tangent to the cable center line, $\boldsymbol{M_c}$ the resultant internal moment, and $\boldsymbol{F_c}$ the external load per unit arc length due to the self-weight $\rho_c g$, and $\boldsymbol{F}_n$, $\boldsymbol{F}_\tau$ and $\boldsymbol{F}_q$ the normal, tangential and bi-normal drag forces (Morrison *et al*. 1950).

3. A 1/100 scale model and experimental setup

A 1/100 scale model of spar-type floating offshore wind turbine is represented in Fig. 3, where wind tower and floating platform are manufactured with hollow aluminum alloy while three rotor blades are made by rapid prototyping (RP) with ABS (acrylonitrile butadiene styrene) copolymer. The thicknesses of wind tower and platform in the structure of hollow cylinder are equally 2.0 mm, and the wind tower is tapered with the slope angle of 19.09°. A 24V DC motor with a built-in encode is mounted on the nacelle and three rotor blades are assembled to the motor shaft by means of a hub. The specification of DC motor was determined by scaling down the rotor of NREL 5MW wind turbine (Wayman *et al*. 2006, Naqvi 2012). The rotor shaft is tilted by 4.0° in order to avoid

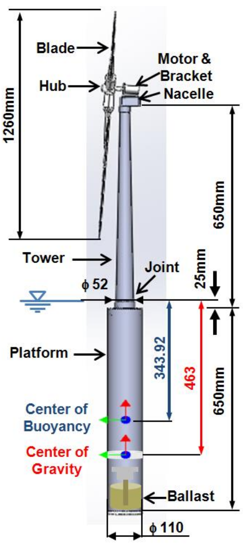

Fig. 3 A 1/100 scale model of spar-type floating offshore wind turbine

the interference between rotor blades and wind tower. The total height of platform and wind tower is 1,300 mm and the diameter of rotor blades is 1,260 mm. The weight of each component is controlled as smaller as possible such that the total weight of the scale model equals to the buoyancy force that will be produced by the platform in water.

The scale model was designed by referring to 2.5 and 5.0MW wind turbines of NREL (Jain and Agarwal 2003, Lee 2008, Karimirad and Moan 2012, Naqvi 2012). When the water line is set to the position 25 mm above the top surface of platform, as shown in Fig. 3, the buoyancy force of our scale model is calculated to be 6.29 kg. Based on the buoyancy force, the weights of each component are designed as follows: 0.99 kg for the platform, 0.2 kg for the wind tower, 0.47 kg for the upper rotor assembly, and 4.63 kg for the ballast. The ballast manufactured with brass is placed at the bottom of platform to compensate the error of weight at design and manufacturing stages as well as to lower the center of gravity. For the current scale model, the center of gravity is designed to be positioned at 119.08 mm below the center of buoyancy. The profile of rotor blades was designed by simply scaling down a NACA 2412 airfoil, not by applying the similarity principle based on the Reynolds number (Re). The rotor blades are forced to rotate at the specific RPM to compensate for the insufficient wind load which is supplied by the wind generator.

Fig. 4 represents the experiment apparatus composed of a 1/100 scale model, water tank, mooring and anchor systems and the wind generator. The dimensions of water tank are 2,300 mm width, 1,300 mm depth and 650 mm height, and water is filled almost up to the top surface. The catenary-type mooring lines composed of tiny steel chains are connected to the center of gravity of platform. One is aligned in the lateral direction of water tank while the other two are aligned 120° in the circumferential direction. The total length of mooring line is adjusted such that the angle ϑ_c^B between mooring line and seabed, as shown in Fig. 2(a), becomes to be 35° at the anchor position. The wind generator which is composed of a 8-blade fan of diameter 0.45 m is placed 2.5 m in front of rotor blades, and three wind speeds of 1.32, 2.5 and 3.5 m/sec in front of the rotor blade are controlled by keeping the rotation speed of fan motor be 420, 600 and 750 rpm, respectively. Three wind speeds correspond to approximately 11.4, 21.6 and 30.1 m/sec in case of real 2.5MW wind turbine (Naqvi 2012).

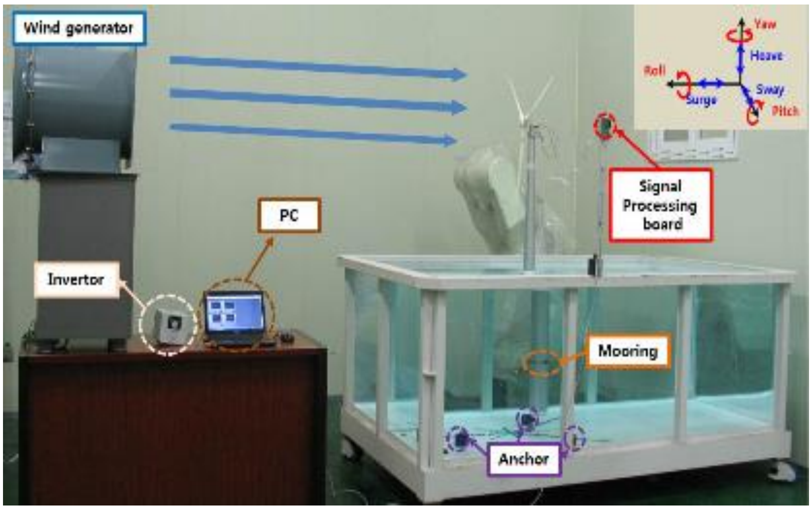

Fig. 4 Apparatus for the scale model experiment

4. Monitoring system for 1/100 scale model

In order to detect and evaluate the dynamic motion of the 1/100 scale mode, a monitoring system shown in Fig. 5 was developed by integrating various sensors, data acquisition system and a real-time controller. The tilting, vibration and force of nacelle are detected by 3-axis inclinometer and accelerometer, while the attitude, angular velocity and acceleration of platform are measured by 3-axis accelerometer, gyroscope and magnetic sensor that are attached to the center of gravity. The sensor signals are collected by a main board and transferred to a host system that is composed of a real-time controller (CompactRIO) and monitoring program. The transferred signal data are processed and filtered to obtain the tilting angle and vibration of nacelle and the attitude, rotation angle and acceleration of platform. In addition, the rotation speed of rotor is controlled by PWM (pulse width modulation) and confirmed by a built-in encoder, in order to maintain the similar conditions to the real wind turbine.

Fig. 6 represents a signal processing algorithm which is embedded into a real-time controller CompactRIO to calculate 3-axis tilting angles and accelerations of nacelle. The measured signal data are averaged and go through the calibration and correction process, and then the direction-wise tilting angles and accelerations of nacelle are finally calculated. Meanwhile, the rigid-body translation and rotation of the platform are calculated using the signals of 3-axis accelerometer, gyroscope and magnetometer that are attached to the center of gravity.

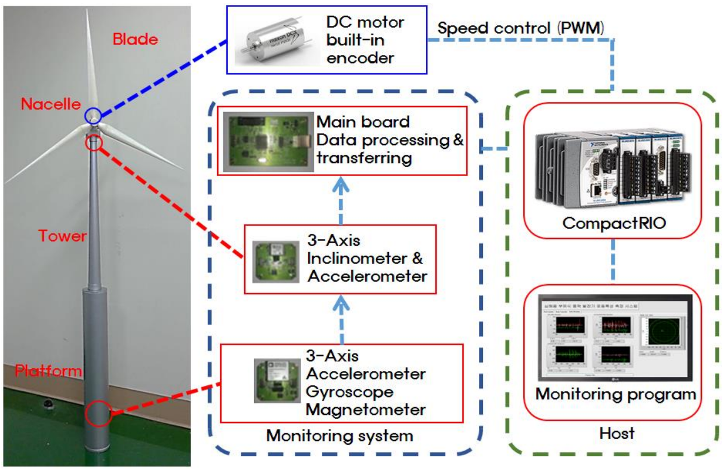

Fig. 5 Monitoring system composed of sensors, signal processor and filter and real-time contrpller

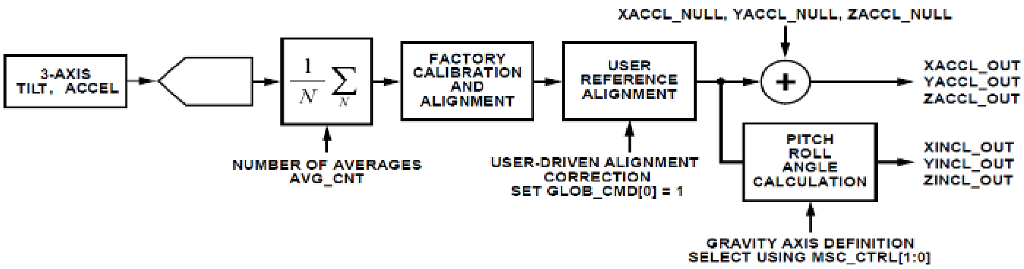

Fig. 6 Signal processing algorithm for the acceleration and tilting angle of nacelle

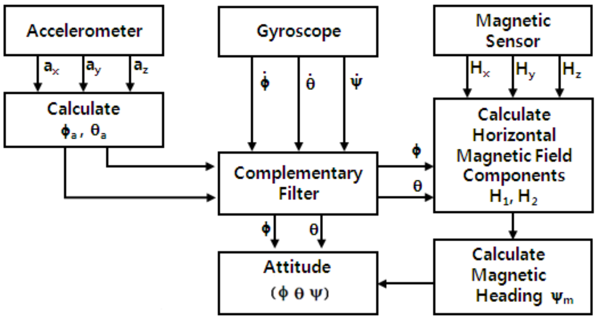

Fig. 7 Calculation procedure of the attitudes $\{\phi, \theta, \psi\}$ of the floating platform

Fig. 7 schematically represents the calculation process of three rotational angles $\{\phi, \theta, \psi\}$ of the platform from the accelerations $\{a_x, a_y, a_z\}$ of accelerometer, the angular accelerations $\{\dot{\phi}_g, \dot{\theta}_g, \dot{\psi}_g\}$ of gyroscope, and the Earth's magnetic heads $\{H_x, H_y, H_z\}$ of magnetometer. In the current study, the roll and pitch angles $\{\phi, \theta\}$ are calculated by making use of the signals of accelerometer and gyroscope, in order to minimize the measuring error of 3-axis accelerometer when the platform is subject to the external load. Meanwhile, the yaw angle ψ is determined using the signal of magnetometer because it cannot be accurately calculated from the signal of accelerometer.

Because the signals of accelerometer are affected by the external load and those of gyroscope are sensitive to the angle change of platform, we apply the low-pass filter (LPF) to the accelerometer and the high-pass filter to the gyroscope. Then, according to the first-order compensation filtering [32], the roll and pitch angles $\{\phi, \theta\}$ are calculated by

$$\phi = \frac{1}{as+1}\phi_a + \frac{as}{as+1}\left(\frac{1}{s}\dot{\phi}_g\right), \quad \theta = \frac{1}{as+1}\theta_a + \frac{as}{as+1}\left(\frac{1}{s}\dot{\theta}_g\right) \tag{5}$$

with ϕ_a and θ_a being $\phi_a = arctan\left(a_y / \sqrt{a_x^2 + a_y^2}\right)$ and $\theta_a = arctan\left(a_x / \sqrt{a_x^2 + a_y^2}\right)$, respectively. Meanwhile, the yaw angle ψ is determined by

$$\psi = arctan(H_2 / H_1) \tag{6}$$

using $H_1 = H_x \cos\theta + H_y \sin\phi \sin\theta + H_z \cos\phi \sin\theta$ and $H_2 = H_y \cos\phi - H_z \sin\phi$ (Shiau and Wang 2013)

Meanwhile, the accelerations $\{a_x, a_y, a_z\}$ measured by the 3-axis accelerometers are the total accelerations including the gravitational force components. The total accelerations and the gravitational force components are in the relation (Hong 2003, Shiau and Wang 2013) given by

$$\begin{Bmatrix} a_x \\ a_y \\ a_z \end{Bmatrix} = \begin{Bmatrix} \dot{v}_x \\ \dot{v}_y \\ \dot{v}_z \end{Bmatrix} + \begin{bmatrix} 0 & v_z & -v_y \\ -v_z & 0 & v_x \\ v_y & -v_x & 0 \end{bmatrix} \begin{Bmatrix} \dot{\phi} \\ \dot{\theta} \\ \dot{\psi} \end{Bmatrix} + g_z \begin{Bmatrix} -\sin\theta \\ \cos\theta\sin\phi \\ \cos\theta\cos\phi \end{Bmatrix} \tag{7}$$

with $\boldsymbol{v} = \{v_x, v_y, v_z\}$ being the translational velocity. Then, three translation components $\{U, V, W\}$ of platform are calculated using Eq. (7), from the measured accelerations $\{a_x, a_y, a_z\}$ and the calculated rotational angles $\{\phi, \theta, \psi\}$.

5. Results

The translational and rotational motions of 1/100 scale model were measured at the nacelle and the center of gravity of platform, with respect to the fairlead position and the wind velocity. Eight fairlead positions, including the center of buoyancy (CB) and the center of gravity (CG), with the uniform interval of 32 mm are taken as shown in Fig. 8(a). The wind velocity is set by 1.32, 2.5 and 3.5 m/sec while the rotational speed of rotor is kept by 120 rpm. Fig. 8(b) represents several different standards for evaluating the time-histories of platform motion. For the current study, five different standards are used: mean, maximum, minimum, upper mean and lower mean, where the last two standards indicate the averages of the upper envelop and the lower envelope, respectively.

5.1 Platform motion

Figs. 9(a)-9(c) represent the transient responses of surge, sway and heave motions of floating platform for the wind velocity V_w of 2.50 m/sec and the fairlead position 5. The translation motions of platform were measured at the center of gravity (CG), as mentioned earlier. Since one of mooring lines is aligned to the opposite direction of wind, the platform tends to tilt clockwise with respect to the *y*-axis (i.e., in the negative pitch direction). Thus, the center of gravity below the fairlead position 5 vibrates in the surge direction with respect to its mean surge that is moved forward. Here, it is worth to note that the mean surge of CG is definitely influenced by the fairlead position, as will be represented in Fig. 10(a).

Meanwhile, it is observed that the amplitude of sway response is almost half of the surge amplitude, which is because the wind direction is aligned to the surge direction. It is also observed that the platform vibrates in the sway direction with the positive mean value, because the platform tends to roll in the direction opposite to the rotor blade rotation while resisting to the mooring

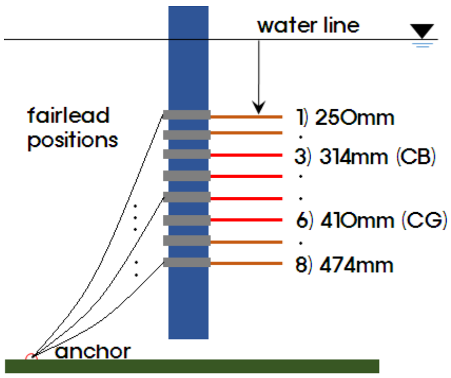

(a)

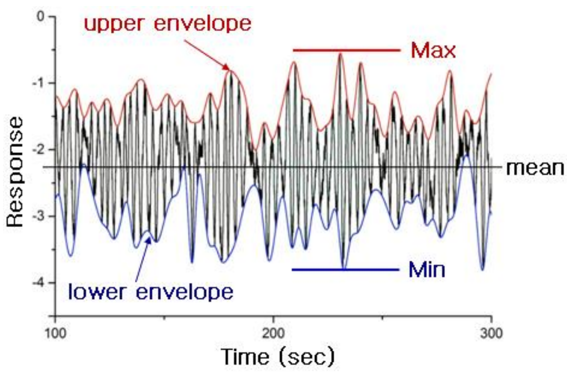

(b)

Fig. 8 (a) Fairlead positions, (b) five different evaluation standards

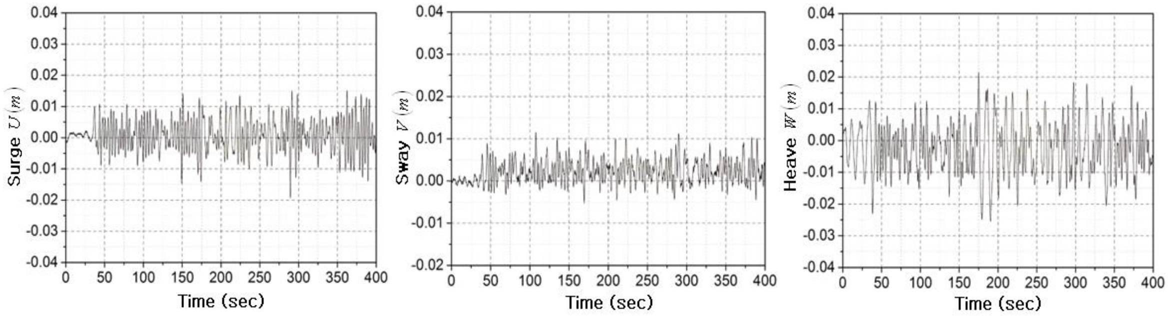

(a) (b) (c)

Fig. 9 Time histories of platform translational motion (wind velocity: $2.50 m/sec$, fairlead position: 5): (a) surge, (b) sway, (c) heave

tension. However, because the resisting moment by the mooring tension increases in proportional to the distance between the fairlead position and the rotor blade axis (Karimirad *et al*. 2011), the positive mean sway decreases as the fairlead position goes downward, as is represented in Fig. 11(a). On the other hand, the heave amplitude is shown to be much larger than the sway amplitude, and even it is observed to be larger than the surge amplitude. It is because the platform tilting (i.e., pitching) causes the coupled heave motion (Choi *et al*. 2016) and the small rigidity of spar-type floating platform that is owing to the relatively small cut water plane area produces large heave motion (Karimirad *et al*. 2011).

Fig. 10(a) represents the variation of mean surge $\bar{U}$ to the fairlead position for three different wind velocities. The mean surge amount is found to be negatively largest at fairlead position 1 for all three wind velocities. But, it decreases to zero as the fairlead position goes downward to 4 (i.e., the position just below the center of buoyancy (BC)), and then it changes to the positive value as the fairlead position further moves downward lower than the position 4. It is because the platform not only moves backward but also tends to tilt by the action of wind. In other words, the combination of backward movement and the clockwise tiling results in the apparent difference in the mean surge amount to the wind velocity for the upper fairlead positions but it does not for the lower fairlead positions. Meanwhile, the mean sway $\bar{V}$ in Fig. 11(a) shows almost the uniform decrease as the fairlead position moves downward because the resisting moment by the mooring tension to suppress the platform tilting becomes larger, as explained above. It is also found that the influence of wind velocity on the mean sway amount becomes smaller as the fairlead position moves downward. Fig. 10(b) represents the difference between the upper and lower means in the transient responses of platform surge. Except for the fairlead position 7, the difference increases with the wind velocity. This trend is also observed from Fig. 11(b) for the transient sway response. It is attributed to the fact that the surge motion of platform becomes unstable at the fairlead position near the center of gravity (Jeon *et al*. 2013). Meanwhile, from Figs. 10(c) and 11(c), it is observed that the differences in the maximum and minimum in both the surge and sway responses uniformly increases with the wind velocity.

Meanwhile, it is observed from Fig. 12(a) that the mean heave of platform becomes unstable as the fairlead position moves downward. It is caused by the unstable surge motion near the fairlead position 7 as observed from Fig. 10. On the other hand, from Figs. 12(a)-12(c), it is not found any consistency in the effect of wind velocity on the heave motion.

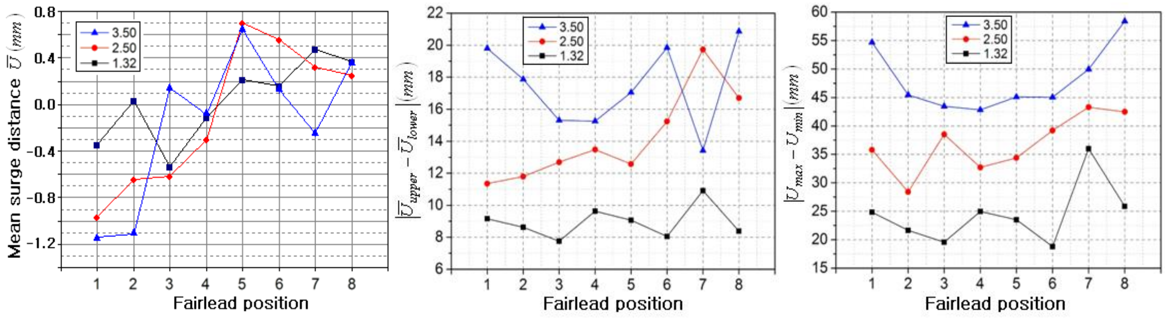

(a) (b) (c)

Fig. 10 Variation of platform surge: (a) mean value $\bar{U}$, (b) difference between the upper and lower means $|\bar{U}_{upper} - \bar{U}_{lower}|$, (c) difference between the maximum and minimum $|U_{max} - U_{min}|$

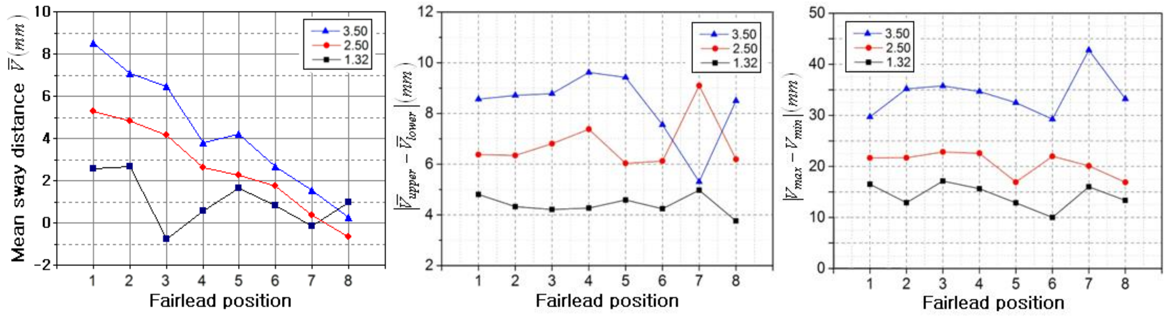

(a) (b) (c)

Fig. 11 Variation of platform sway: (a) mean value $\bar{V}$, (b) difference between the upper and lower means $|\bar{V}_{upper} - \bar{V}_{lower}|$, (c) difference between the maximum and minimum $|V_{max} - V_{min}|$

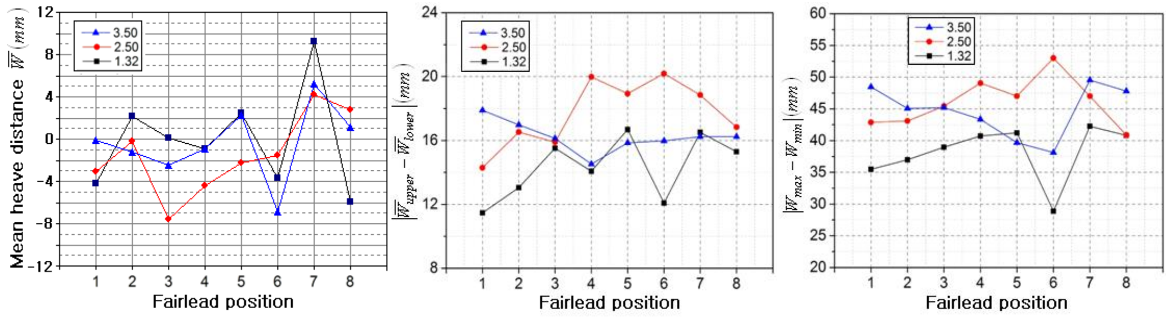

(a) (b) (c)

Fig. 12 Variation of platform heave: (a) mean value $\bar{W}$, (b) difference between the upper and lower means $\bar{W}_{upper} - \bar{W}_{lower}$, (c) difference between the maximum and minimum $W_{max} - W_{min}$

Figs. 13(a)-13(c) represent the transient responses of roll, pitch and yaw motions for the wind velocity V_w of 2.50 m/sec and the fairlead position 4. It is found that the yaw angle is much larger than roll and pitch angles, because the yaw motion is sensitive to the unbalance of wind pressure

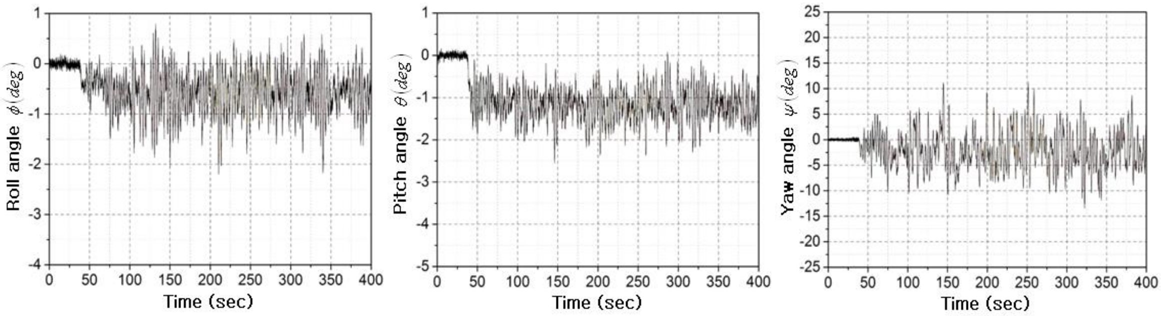

(a) (b) (c)

Fig. 13 Time histories of platform rotational motion (wind velocity: 2.50 m/sec, fairlead position: 4): (a) roll, (b) pitch, (c) yaw

distribution on three rotor blades that is caused by the non-uniform sectional wind velocity profile and the misalignment of the rotor and wind generator axes. Furthermore, the rotational resistance to the yaw motion by three mooring lines is relatively smaller than those to the roll and pitch motions.

Fig. 14(a) shows the variation of mean roll angle to the fairlead position for three different wind velocity, where the roll angle is relatively smaller for the fairlead positions between 3 and 5. In other words, the roll motion is more suppressed when the fairlead is positioned between CB and CG. This trend is also found from the mean pitch angle shown in Fig. 15(a), and furthermore it is also observed that the pitch angle decreases as the fairlead position moves downward, particularly for higher wind velocity. It is because the pitch stiffness increases in proportional to the distance between the rotor axis and the fairlead position (Karimirad *et al*. 2011). For all the fairlead positions, it is observed that the wind velocity gives rise to the consistent effect on the mean value and two difference values of roll and pitch angles, with respect to the wind velocity. In other words, three quantities $\bar{\phi}$, $\left|\bar{\phi}_{upper} - \bar{\phi}_{lower}\right|$ and $\left|\phi_{max} - \phi_{min}\right|$ uniformly increase in proportional to the wind velocity.

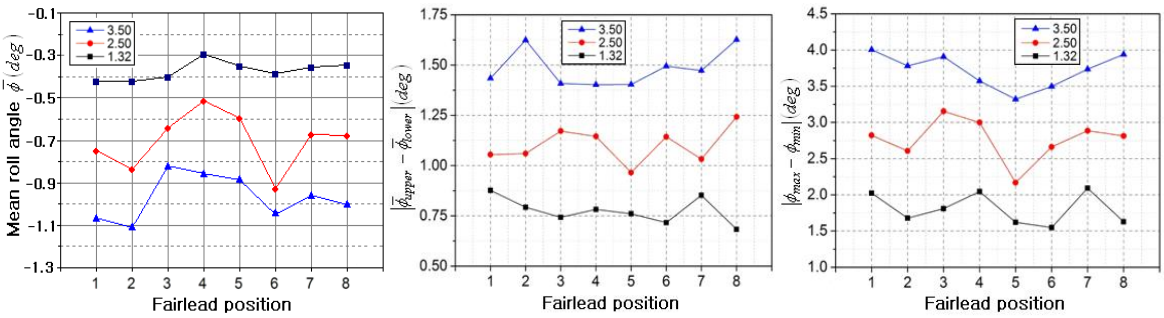

(a) (b) (c)

Fig. 14 Variation of platform roll: (a) mean value $\bar{\phi}$, (b) difference between the upper and lower means $\left|\bar{\phi}_{upper} - \bar{\phi}_{lower}\right|$, (c) difference between the maximum and minimum $\left|\phi_{max} - \phi_{min}\right|$

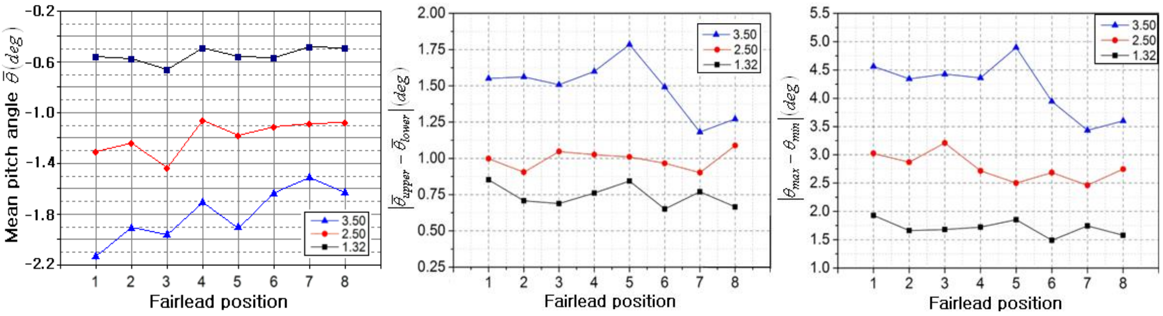

(a) (b) (c)

Fig. 15 Variation of platform pitch: (a) mean value $\bar{\theta}$, (b) difference between the upper and lower means $\left|\bar{\theta}_{upper} - \bar{\theta}_{lower}\right|$, (c) difference between the maximum and minimum $\left|\theta_{max} - \theta_{min}\right|$

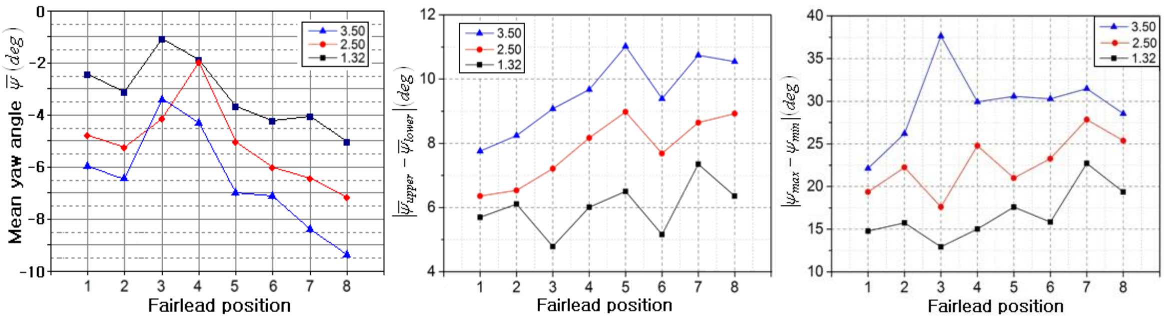

(a) (b) (c)

Fig. 16 Variation of platform yaw: (a) mean value $\bar{\psi}$, (a) difference between the upper and lower means $\left|\bar{\psi}_{upper} - \bar{\psi}_{lower}\right|$, (c) difference between the maximum and minimum $\left|\psi_{max} - \psi_{min}\right|$

Fig. 16(a) shows the variation of mean yaw of platform to the fairlead position for three different wind velocities, where the mean yaw as a whole increases in proportional to the wind velocity. The trend is also observed at the difference between the upper and lower means shown in Fig. 16(b) and at the difference between the maximum and minimum shown in Fig. 16(c). The mean yaw angle is found to be relatively smaller for the fairlead positions between CB and CG, which is similar to the mean roll angle shown in Fig. 14(a). And, the mean yaw increases as the fairlead position moves upward or moves downward, from the fairlead positions 3 and 4. On the other hand, referring to Figs. 16(b) and 16(c), the difference between the upper and lower means and the difference between the maximum and minimum as a whole increase as the fairlead position moves downward. In aspect of the mean yaw, it has found that the fairlead position between CB and CG is preferable to suppress the platform rotational motion.

5.2 Nacelle tilting and motion trajectories

Next, the roll and pitch responses of nacelle are investigated in order to examine the difference between the measured rotational data at the center of gravity. The yaw response was excluded

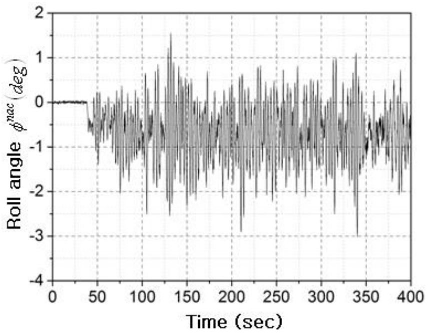

(a)

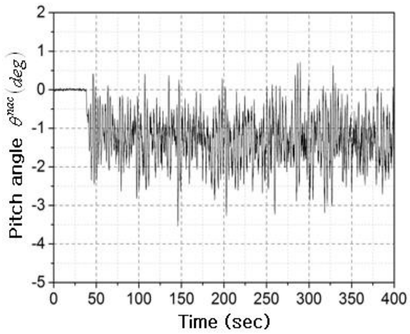

(b)

Fig. 17 Time histories of nacelle rotational motion (wind velocity: 2.50 m/sec, fairlead position: 4): (a) roll, (b) pitch

because only 3-axis inclinometer and accelerometer are installed at nacelle and the yaw responses measured using these sensors are not accurate. Remind that the yaw response of platform was measured by attaching 3-axis magnetometer to the center of gravity. The transient responses of nacelle roll and pitch are represented in Figs. 17(a) and 17(b), and their counterpart responses are the previous Figs. 13(a) and 13(b). Except for the difference in the peak responses, it is hard to find the difference in the overall response time histories. In both cases of roll and pitch responses, the peak responses at nacelle are observed to be about 1.4 times as high as ones at the center of gravity. This discrepancy is assumed to be caused by the difference between inclinometer at nacelle and gyroscope at platform. In addition, the use of compensation filter for platform is also assumed to cause the discrepancy.

The variations of mean roll and pitch angles to the fairlead position for three different wind velocities are represented in Figs. 18(a) and 18(b). By comparing with the previous Figs. 14(a) and 15(a) at the center of gravity of platform, one can find out that both cases show the overall variations similar to each other. In the roll response, both cases show the noticeable difference at fairlead positions 3~6, and the maximum relative difference is found to be 27.8% at fairlead position 6. Meanwhile, in the pitch response, the measurement at nacelle leads to smaller angle as a whole, and this trend becomes more apparent in proportional to the wind velocity. The maximum relative difference is found to be 16.5% at fairlead position 6 when the wind velocity V_w is 1.32 m/sec. This difference is also assumed to be attributed to the above-mentioned reason. Even though the plots are not included in this paper, both the difference between the upper and lower means and the difference between the maximum and minimum in the nacelle roll and pitch responses lead to the almost similar difference to the mean roll and the mean pitch.

Fig. 19 represents the trajectories of nacelle during 400 sec for three different wind velocities when the fairlead position is located at position 4. The trajectories were obtained by our monitoring system shown in Fig. 5, which clearly justifies the usefulness of monitoring system that one can easily figure out the nacelle tilting characteristics at a glance. It is observed that the nacelle shows a typical umbrella-like trajectory, and it was observed that the trajectories are slightly different for different fairlead positions. It is found that the nacelle position is tilted as a whole in the positive *x*- and *y*- directions, which is consistent with the previous mean roll $\bar{\phi}^{nc}$ and pitch $\bar{\theta}^{nc}$ of nacelle shown in Fig. 18. In other words, the nacelle motion prevails in the negative roll and pitch directions.

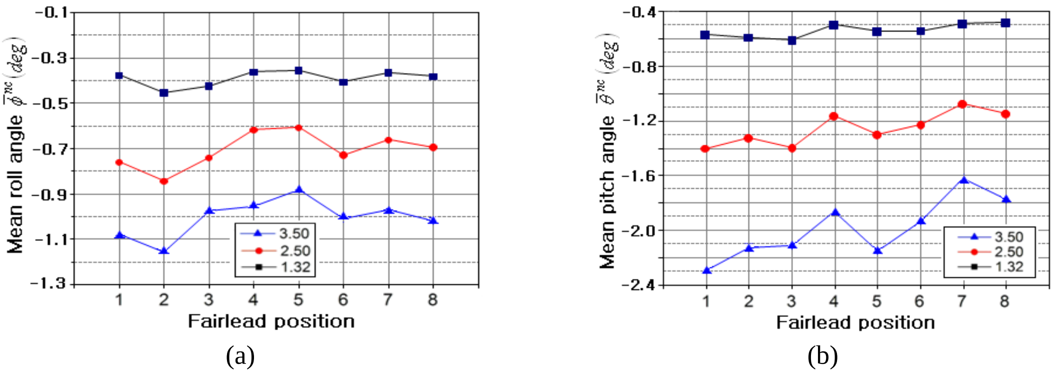

Fig. 18 (a) Nacelle mean roll $\bar{\phi}^{nc}$, (b) nacelle mean pitch $\bar{\theta}^{nc}$

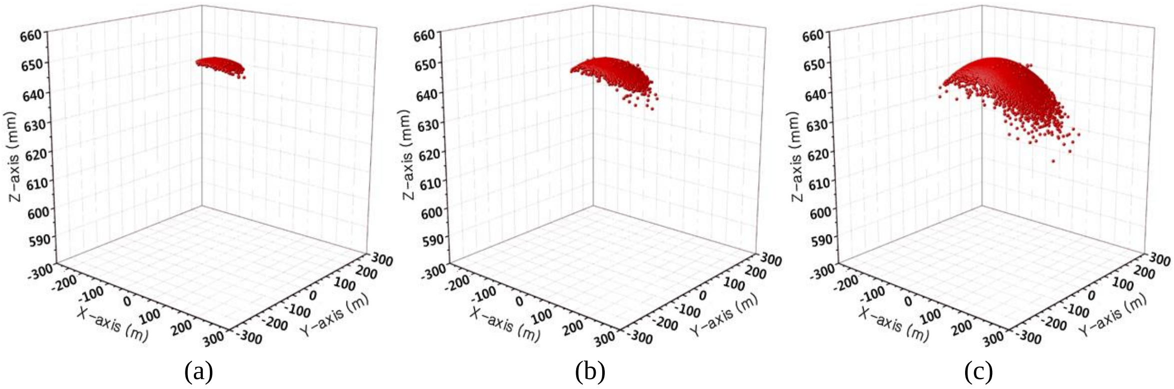

Fig. 19 Trajectories of nacelle to the wind velocity (fairlead position: 4): (a) 1.32 m/sec, (b) 2.50 m/sec, (c) 3.50 m/sec

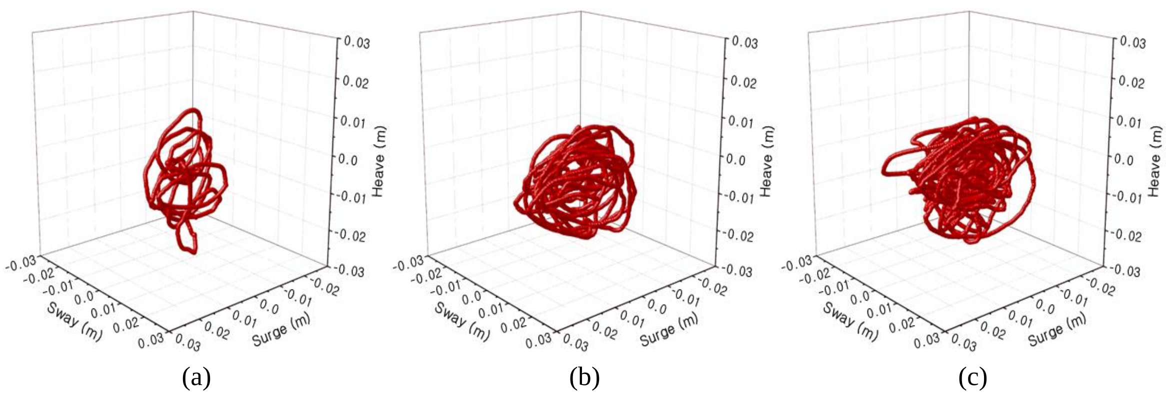

Fig. 20 Trajectories of platform at the center of gravity (wind velocity: 2.50 m/sec, fairlead position: 5): (a) 0~70 sec, (b) 70~140 sec, (c) 140~280 sec

Fig. 20 represents the time interval-wise trajectories of the center of gravity (CG) of platform at the wind velocity of V_w=2.5 m/sec for the fairlead position 5. In the early stage, it is found that the platform motion is dominated by the heave motion, which is consistent with the time histories of platform motion shown in Fig. 9. After that, the platform shows almost the sphere-like trajectory according to the active surge and sway motions. We observed that the evolution of platform trajectory with the lapse of time is also almost the same for different wind velocities and different fairlead positions. It implies that the trajectory evolution shown in Fig. 20 is a peculiar motion characteristic of the spar-type floating platform subject to the wind load as shown Fig. 4. Thus, the monitoring system developed through the current study provides the useful dynamic characteristics of the scale model of spar-type floating offshore wind turbine, such as the time histories of translational and rotational motions and the motion trajectories and their evolution.

6. Conclusions

In this paper, a monitoring system for a 1/100-scale spar-type floating offshore wind turbine has been developed and demonstrated. The system was developed by integrating a 1/00 scale model, water basin equipped with the wind generator, sensing and data acquisition systems and real-time CompactRIO controller. The translational and rotational motions of platform were measured by 3-axis accelerometer, magnetometer and gyroscope and processed by utilizing the first-order compensation filter. Meanwhile, the nacelle tilting was measured by 3-axis inclinometer and accelerometer and averaged and calibrated by a signal processing algorithm. Using the developed monitoring system, the time histories and trajectories of nacelle and platform were measured and evaluated for three different wind velocities and eight different fairlead positions.

In case of the platform motion, the developed system provides the parametrically consistent dynamic characteristics of translational and rotational motions to the wind velocity and fairlead position. The coupling between platform tilting and heave motion was successfully detected and the effects of fairlead position and wind velocity were found to be consistent from the evaluation of correlation between six components of platform motion. The trajectories of platform and their evolution with the lapse of time were also easily figured out. In case of the nacelle tilting, the system provides the roll and pitch responses that are similar to the platform tilting. Meanwhile, the measurement showed the maximum relative difference at the fairlead position 6. The system also provides the nacelle trajectories that are useful to figure out the overall nacelle tilting at a glance.

Through the illustrative demonstration, it has been justified that the developed monitoring system successfully provides the sufficient dynamic information of spar-type floating offshore wind turbine that is essential for investigating the motion characteristics of nacelle and platform.

Acknowledgements

This work was supported by the Korea Institute of Energy Technology Evaluation and Planning(KETEP) and the Ministry of Trade, Industry & Energy(MOTIE) of the Republic of Korea (No. 20168520021200). This work was also supported by 2016 Hongik University Research Fund.

References

Aamo, O.M. and Fossen, T.I. (2000), “Finite element modeling of mooring lines”, *Math. Comput. Simulat.*,

53(4-6), 415-422.
Breton, S.P. and Noe, G. (2009), "Status, plans and technologies for offshore wind turbines in Europe and North America", *Renew. Energy*, **34**(3), 646-654.
Choi, E.Y., Jeong, W.B. and Cho, J.R. (2016), "Combination resonances in forced vibration of spar-type floating substructure with nonlinear coupled system in heave and pitch motion", *Int. J. Naval Architect. Ocean Eng.*, **8**(3), 252-261.
Choi, E.Y., Cho, J.R., Cho, Y.U., Jeong, W.B., Lee, S.B., Hong, S.P. and Chun, H.H. (2015), "Numerical and experimental study on dynamic response of moored spar-type scale platform for floating offshore wind turbine", *Struct. Eng. Mech.*, **54**(5), 909-922.
Cowell, S. and Basu, B. (2009), "Tuned liquid column dampers in offshore wind turbines for structural control", *Eng. Struct.*, **31**(2), 358-368.
Faltinsen, O.M. (1990), *Sea Load on Ships and Offshore Structures*, University of Cambridge.
Frye, J., Horvath, N. and Ndegwa, A. (2011), *Design of Scale-Model Floating Wind Turbine: Spar Buoy, Project Report*, Worcester Polytechnic Institute.
Goodman, T.R. and Breslin, J.P. (1976), "Statics and dynamics of anchoring cables in waves", *J. Hydronaut*, **10**(4), 113-120.
Hong, S.K. (2003), "Fuzzy logic based closed-loop strapdown attitude system for unmanned aerial vehicle (UAV)", *Sensors Actuators A*, **107**(2), 109-118.
Jain, A.K. and Agarwal, A.K. (2003), "Dynamic analysis of offshore spar platforms", *Defence Sci. J.*, **53**(2), 211-219.
Jeon, S.H., Cho, Y.U., Seo, M.W., Cho, J.R. and Jeong, W.B. (2013), "Dynamic response of floating substructure of spar-type wind turbine with catenary mooring cables", *Ocean Eng.*, **72**, 356-364.
Jonkman, J.M. (2009), "Dynamics of offshore floating wind turbines-model development and verification", *Wind Energy*, **12**(5), 459-492.
Jonkman, J.M. and Buhl, M.L. (2007), "Loads analysis of a floating offshore wind turbine using fully coupled simulation", *NREL/CP-500-41714*.
Karimirad, M. (2014), "Floating offshore wind turbines", *Offshore Energy Struct.*, 54-76.
Karimirad, M. and Moan, T. (2012), "Wave- and wind-induced dynamic response of a spar-type offshore wind turbine", *J. Waterway Port Coast. Ocean Eng.*, **138**(1), 9-20.
Karimirad, M., Meissonnier, Q., Gao, Z. and Moan, T. (2011), "Hydroelastic code-to-code comparison for a tension leg spar-type floating wind turbine", *Marine Struct.*, **24**(2), 412-435.
Koo, B.J., Kim, M.H. and Randall, R.E. (2004), "Mathieu instability of a spar platform with mooring and risers", *Ocean Eng.*, **31**(17), 2175-2208.
Lee, K.H. (2005), "Response of floating wind turbines to wind and wave excitation", Masters Thesis, MIT.
Lee, S.H. (2008), "Dynamic response analysis of spar buoy floating wind turbine systems", Ph.D. Thesis, MIT.
Martin, H.R. (2011), "Development of a scale model wind turbine for testing of offshore floating wind turbine systems", Master Thesis, The University of Maine.
Morison, J.R., O'Brien, M.P., Johnson, J.W. and Schaaf, S.A. (1950), "The force exerted by surface waves on piles", *J. Petroleum Technol.*, **2**(05), 149-157.
Musial, W. and Butterfield, S. (2004), "Future for offshore wind energy in the United States", *NREL/CP-500-36313*.
Naqvi, S.K. (2012), "Scale model experiments on floating offshore wind turbines", Master Thesis, Worcester Polytechnic Institute.
Nielson, F.G., Hanson, T.D. and Skaare, B. (2006), "Integrated dynamic analysis of floating offshore wind turbine", *Proceeding of the 25th Int. Conf. Offshore Mech. Arctic Eng. (OMAE2006)*, **1**, 671-679.
Shiau, J.K. and Wang, I.C. (2013), "Unscented Kalman filtering for attitude determination using MEMS sensors", *J. Appl. Sci. Eng.*, **16**(2), 165-176.
Ton, K.C. (1998), "Technical and economic aspects of a floating offshore wind far", *J. Wind Eng. Ind. Aerod.*, **74-76**, 399-410.
Torrance, V.B. (1972), "Wind profiles over a suburban site and wind effects on a half-scale model building",

Build. Sci., **7**(1), 1-12.
Utsunomiya, T., Matsukuma, H., Minoura, S., Ko K., Hamamura, H., Kobayashi, O., Sato, I., Nomoto, Y. and Yasui, K. (2013), "At sea experiment of a hybrid spar for floating offshore wind turbine using 1/10-scale model", *J. Offshore Mech. Arctic Eng.*, **135**(3), 034503.
Waris, M.B. and Ishihara, T. (2012), "Dynamic response analysis of floating offshore wind turbine with different types of heave plates and mooring systems by using a fully nonlinear model", *Coupled Syst. Mech*., **1**(3), 247-268.
Wayman, E.N., Sclavounos, P.D., Butterfield, S., Jonkman, J. and Musial, W. (2006), "Coupled dynamic modeling of floating wind turbine systems", *Offshore Technol. Conf., OTC-18287-MS*, 2006.

CC